ACS OMEGA

http://pubs.acs.org/journal/acsodf

Article

Catalytic Oxidation of *n*-Decane, *n*-Hexane, and Propane over Pt/CeO_2 Catalysts

Xiaohui Gao, Yuting Bai, Hao Zhang, and Xingyi Wang*

Cite This: *ACS Omega* 2023, 8, 6791−6800

Read Online

ABSTRACT: Pt species with different chemical states and structures were supported on CeO_2 by solution reduction (Pt/CeO_2-SR) and wet impregnation (Pt/CeO_2-WI) and investigated in catalytic oxidation of *n*-decane ($C_{10}H_{22}$), *n*-hexane (C_6H_{14}), and propane (C_3H_8). Characterization by X-ray diffraction, Raman spectroscopy, X-ray photoelectron spectroscopy, H_2-temperature programming reduction, and oxygen temperature-programmed desorption showed that Pt^0 and Pt^{2+} existed on Pt nanoparticles of the Pt/CeO_2-SR sample, which promoted redox, oxygen adsorption, and activation. On Pt/CeO_2-WI, Pt species were highly dispersed on CeO_2 as the Pt−O−Ce structure, in which surface oxygen decreased significantly. The Pt/CeO_2-SR catalyst presents high activity in oxidation of $C_{10}H_{22}$ with a rate of 0.164 μmol min^{-1} m^{-2} at 150 °C. The rate increased with oxygen concentration. Moreover, Pt/CeO_2-SR presents high stability on feed stream containing 1000 ppm $C_{10}H_{22}$ at gas hour space velocity = 30,000 h^{-1} as low as 150 °C for 1800 min. The low activity and stability of Pt/CeO_2-WI were probably related to its low availability of surface oxygen. In situ Fourier transform infrared results showed that the adsorption of alkane occurred through the interaction with Ce−OH. The adsorption of C_6H_{14} and C_3H_8 was much weaker than that of $C_{10}H_{22}$, which resulted in the decrease in activity for C_6H_{14} and C_3H_8 oxidation of Pt/CeO_2 catalysts.

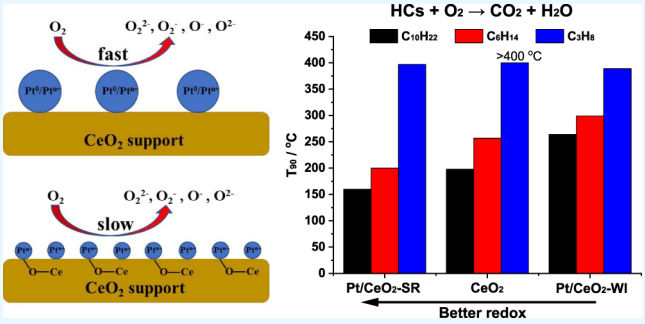

1. INTRODUCTION

Volatile organic compounds (VOCs) are considered to be a major source of air pollution, mainly from unburned hydrocarbons (HCs), certain industrial workplaces,[1] and automotive engines.[2] These compounds contribute to the greenhouse effect and photochemical smog.[3] Catalytic combustion is the most promising technology for eliminating VOCs, due to its low reaction temperature and low energy consumption compared to thermal technology.[4]

The common hydrocarbon oxidation catalysts are platinum group metals (Pt, Pd, Ru, Rh, Ag)[5−7] and transition metal oxides (CeO_2, MnO_2, Co_3O_2, Fe_2O_3).[8−10] Among them, Pt catalysts possess high activity, due to their excellent ability to activate oxygen and C−H bonds except methane oxidation, in which Pd is more suitable. Santos et al.[11] compared the activity of noble metal catalysts supported on TiO_2 for ethanol and toluene oxidation and found the activity order to be Pt/TiO_2 ∼ Rh/TiO_2 > Pd/TiO_2 > Au/TiO_2 ∼ TiO_2. Specific activities depend on O_2 adsorption strengths on metals. Gololobov[12] found that the catalytic activity of Pt/Al_2O_3 for total oxidation of C_1−C_6 *n*-alkanes was promoted with the increase in the Pt particle size. In total oxidation of *n*-decane and 1-methylnaphthalene,[13] the Pt/Al_2O_3 catalyst with 0.39 Pt dispersion presented high activity. However, the increase in Pt dispersion was not favorable for the activity of Pt/ZrO_2 catalysts. Fabrice[14] found that the reactivity of *n*-alkane on the Pt/Al_2O_3 catalyst increases with the carbon atoms. In methane oxidation, the reaction rate increased and the reaction order changed from zero-order to negative-order in the oxygen partial pressure during decreasing O_2/CH_4 ratio.[15] The O_2/alkane ratio at the maximum rate for C_2H_6 oxidation was higher than that for CH_4 oxidation, due to the difference in the consumption of chemisorbed oxygen.[16] In the case of propane oxidation, Pt species were saturated with oxygen at high O_2/C_3H_8 ratios, and thus the reaction rate was zero-order with respect to the oxygen partial pressures.[17,18] Hasan compared the oxidation of propane on ZrO_2, TiO_2, and CeO_2 catalysts and found that the activity of CeO_2 was higher than that of Pt/Al_2O_3 catalyst.[19] As is known, CeO_2 has high oxygen storage capacity, due to quick transformation between Ce^{4+} and Ce^{3+} states under reductive and oxidative conditions.[20] Thus, Pt catalysts on CeO_2-based supports were widely used in various reactions, such as the water gas shift reaction[21] and catalytic oxidation.[22] At present, the relation among the catalytic

Received: November 18, 2022
Accepted: January 26, 2023
Published: February 8, 2023

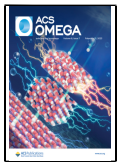

Table 1. Structure and Physicochemical Properties of Pt/CeO_2 Samples

sample	S_{BET}[a]/m^2 g^{-1}	Pt loading[b]/wt %	Pt dispersion[c]/%	Pt size/nm		Pt composition/at %		
				CO[d]	XRD[e]	Pt^0	Pt^{2+}	Pt^{4+}
CeO_2	116							
Pt/CeO_2-SR	98	0.91	5	20.6	24.7	44.0	46.7	9.3
Pt/CeO_2-WI	101	0.97	37	2.8	n.d.[f]	0	75.9	24.1

[a]Determined from the N_2 adsorption isotherm. [b]Obtained by ICP-AES. [c]Measured by pulsed CO chemisorption at −50 °C. [d]Calculated by the method reported by the literature.[24] [e]Crystallite size estimated by the Scherrer equation, applied to the (111) plane of Pt. [f]n.d. No data can be calculated partially because the particle is too small.

performance and structure of Pt/CeO_2 catalysts and catalytic activity for the oxidation of *n*-alkanes with different numbers of carbon atoms needs to be still investigated. In this work, Pt/CeO_2-SR and Pt/CeO_2-WI catalysts were prepared by solution reduction and wet impregnation. Using the oxidation of *n*-decane ($C_{10}H_{22}$), *n*-hexane (C_6H_{14}), and propane (C_3H_8) as model reactions, the relation between the surface performance of Pt/CeO_2 and catalytic activity was studied.

2. RESULTS AND DISCUSSION

2.1. Characterization of Catalysts. The nitrogen adsorption/desorption isotherms and pore size distributions of samples are presented in Figure S1. All samples show the classical shape of an IV-type isotherm. The Brunauer−Emmett−Teller (BET) area of the CeO_2 sample is estimated to be 116 m^2/g (Table 1) and decreases to 98−101 m^2/g after loading Pt. Figure 1 shows X-ray diffraction (XRD) patterns of

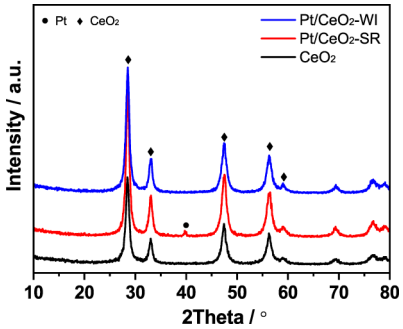

Figure 1. XRD patterns of Pt/CeO_2 samples.

samples. The diffraction peaks appearing at 28.6, 33.3, 47.5, 56.5, and 59.2° are ascribed to <111>, <200>, <220>, <311>, and <400> crystal planes of cubic fluorite CeO_2, respectively (PDF #34-0394). For the Pt/CeO_2-SR sample, a new peak at 39.8° corresponds to metal Pt <111>.[23] However, no diffraction peak of crystal Pt is observed for the Pt/CeO_2-WI sample, suggesting that Pt species are highly dispersed into CeO_2. Pt content was determined by ICP-AES to be 0.97 and 0.91 wt % for Pt/CeO_2-WI and Pt/CeO_2-SR samples, respectively. Additionally, the former presents 37% Pt dispersion, and the latter, 5%, which suggests that Pt species of the Pt/CeO_2-SR sample exist as Pt nanoparticles. Transmission electron microscopy (TEM) and high-resolution transmission electron microscopy (HRTEM) images of the samples (Figure S2) show that small CeO_2 particles aggregate into a large plane with the lattice spacing of 0.32 nm, corresponding to the <111> plane of CeO_2 (JCPDS 34−0394). With Pt addition, the samples present similar morphology. HAADF-STEM-EDX element-mapping analyses (Figure S3a,b) show that the average size of Pt nanoparticles on the Pt/CeO_2-SR sample is about 30 nm nanoparticles, consistent with XRD results (Table 1). For the Pt/CeO_2-WI sample, Pt species are highly dispersed on the CeO_2 surface (Figure S3c,d).

2.2. Raman Spectra. Before recording spectra, the samples were pretreated with He flow for 1 h at 400 °C, following the treatment with 5% O_2/Ar flow (30 mL/min) for 30 min at 100 °C. As shown in Figure 2, a prominent band at 460 cm^{-1} can

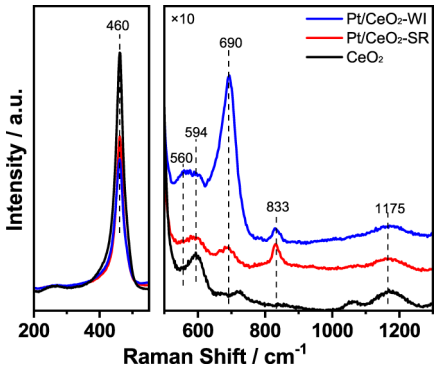

Figure 2. Raman spectra of Pt/CeO_2 samples.

be attributed to triply degenerate F_{2g} mode of CeO_2 with the fluorite structure, while the peaks at 594 and 1175 cm^{-1} are assigned to defect-induced (*D*) mode and second-order longitudinal optical (2LO) mode of CeO_2, respectively.[25] With Pt addition, these bands become weak and broad, and there appear two additional bands at 560 and 690 cm^{-1}, which can be attributed to the bridging Pt−O−Ce and Pt−O of Pt−O−Ce, respectively.[26] Metallic Pt is not Raman-active.[27] Neither amorphous PtO_2 (610 cm^{-1}) nor crystalline PtO (438 cm^{-1} (E_g)), 657 cm^{-1} (B_{1g})) appears.[27] The intensity of Pt−O−Ce bonds is much stronger for Pt/CeO_2-WI, although $Pt^{\delta+}$ content in the Pt/CeO_2-SR sample is 56.0% (calculated based on X-ray photoelectron spectroscopy (XPS) data, Table 1). This phenomenon indicates that Pt species on Pt/CeO_2-WI exist mainly in the form of Pt−O−Ce bonds. In other words, there exists a strong metal-support interaction between Pt and CeO_2, but the ionic state Pt on the surface of the Pt/CeO_2-SR sample mainly exists in the aggregation state. There should appear two bands at 833 and 1175 cm^{-1} which can be ascribed to peroxide (O_2^{2-}) species and superoxide (O_2^-), due to them being Raman-active.[28] In this test, almost no band at 833 cm^{-1} on CeO_2 appears, probably due to the desorption of reversibly adsorbed peroxy-like species. The band at 833 cm^{-1} becomes strong with Pt loading (Figure 2), probably because Pt in contact with the CeO_2 domain promotes the formation of O_2^{2-}, especially for Pt/CeO_2-SR. In contrast, there is no significant change in the ratio of I_{1175}/I_{460} (Table S1),

https://doi.org/10.1021/acsomega.2c07399
ACS Omega 2023, 8, 6791−6800

indicating that superoxide (O_2^-) species come mainly from CeO_2.

2.3. Chemical States. XPS spectra of Pt 4f, Ce 3d, and O 1s for the samples are shown in Figures 3a and S4. There are

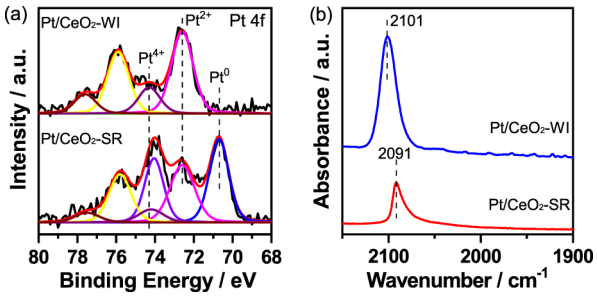

Figure 3. XPS spectra of Pt 4f for Pt/CeO_2 samples (a) and Fourier transform infrared (FTIR) spectra of CO-adsorption (b).

two Pt species on the surface of the Pt/CeO_2-WI sample with a binding energy (BE) of Pt^{2+} $4f_{7/2}$ and Pt^{2+} $4f_{5/2}$ of 72.6 and 75.8 eV, and BE of Pt^{4+} $4f_{7/2}$ and Pt^{4+} $4f_{5/2}$ of 74.2 and 77.5 eV, respectively.[29] Pt^0 species appear on the surface of the Pt/CeO_2-SR sample with a BE of 70.7 and 74.0 eV,[30] and the ratio of Pt^0/Pt is estimated to be up to 44.0%. While in the Pt/CeO_2-WI sample, Pt exists as Pt^{2+} and Pt^{4+} species, which strongly interacts with CeO_2 to form Pt−O−Ce. IR spectra of CO adsorption on Pt/CeO_2 samples are used to investigate the Pt chemical state (Figure 3b). The linear CO-adsorption peak of Pt/CeO_2-SR at 2091 cm^{-1} is attributed to the reduced Pt, 10 cm^{-1} lower than that on the Pt/CeO_2-WI sample (2101 cm^{-1}). The red shift of linear CO vibrational frequency obviously indicates that the electronic abundance of the loaded Pt over Pt/CeO_2-SR sample is high.[31]

In Ce 3d spectra, the identified peaks with the deconvolution method are caused by the pairs of spin-orbit doublets (Figure S4a). Ce^{4+} contributes to six peaks denoted as v, v'', v''', u, u'', u''', and Ce^{3+}, to peaks as v', and u'.[32] In O 1s spectra (Figure S4b), O 1s peaks are deconvoluted into three peaks at 529.2−529.4, 531.0−531.2, and 533.0−533.2 eV, which are ascribed to lattice oxygen, surface oxygen (O_2^{2-}, O_2^-, O^- species), and oxygen in water, hydroxyl, and CO_2.[33] Here, $O_{surface}$ should not include reversibly adsorbed O_2^{2-} species which is removed due to desorption under XPS ultrahigh vacuum conditions (oxygen temperature-programmed desorption (O_2-TPD) test in Figure 5 confirms significant desorption of O_2^{2-} species at low temperature). Neither the Ce^{3+}/Ce ratio nor the $O_{surface}/O_{total}$ ratio shows significant changes (Table S1).

2.4. H_2-Temperature Programming Reduction (H_2-TPR) and O_2-TPD. H_2-TPR is used to investigate the reducibility of the samples (Figure 4). For the CeO_2 sample, a broad reduction peak appears at 250−580 °C, which can be ascribed to the reduction of surface Ce^{4+} species on small or highly defective nanoparticles (low temperature) and on large CeO_2 particles (high temperature), respectively. With Pt addition, there appears a strong narrow reduction peak at 120 °C for Pt/CeO_2-SR and at 290 °C Pt/CeO_2-WI, respectively, which can be ascribed to the reduction of Ce^{4+} and Pt^{2+} or Pt^{4+} species. The promoted reduction of Ce^{4+} can be ascribed to high ability of Pt species for H_2 dissociation at low temperature. The increase in reduction temperature of Pt/CeO_2-WI should be related to weak H_2 dissociation on Pt^{2+} or

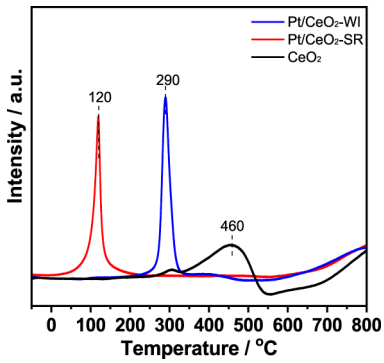

Figure 4. H_2-TPR profiles of Pt/CeO_2 samples.

Pt^{4+} species and to the formation of Pt−O−Ce species with strong metal-support interaction.[34] The corresponding H_2 consumption of two samples is higher than that of theoretical hydrogen consumption (Table S2), which is calculated based on the mole number of H_2 converted for both CeO_2 reduction (normalized by surface Ce^{4+}%) and Pt reduction (Table S2). This phenomenon could be ascribed to the H_2 spillover effect induced by SMSI. It should be noted that the bulk reduction of CeO_2 (higher than 800 °C) is not affected by Pt addition, which is consistent with a previous report that Pt-ceria interaction was limited to the support surface.[35]

O_2-TPD tests were carried out to determine the mobility of oxygen species of Pt/CeO_2 (Figure 5). Generally, the

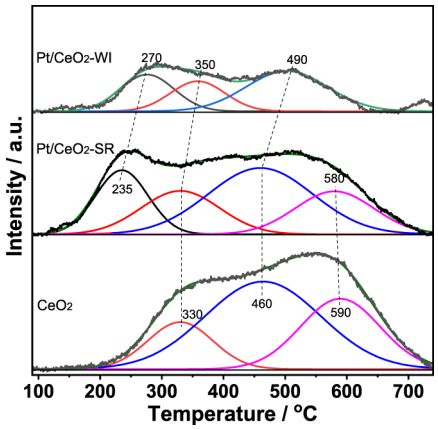

Figure 5. O_2-TPR profiles of Pt/CeO_2 samples.

desorption sequence of surface oxygen species is reversibly and chemically adsorbed oxygen (O_2^{2-}), irreversibly and chemically adsorbed oxygen (O_2^-), surface oxygen (O^-), and surface lattice oxygen (O^{2-}). The O_2-TPD profile of CeO_2 is identified by deconvolution as three desorption peaks with maxima at 330, 460, and 590 °C, which should correspond to the desorption of O_2^-, O^-, and O^{2-}, respectively.[36] For the Pt/CeO_2-SR sample, an additional strong desorption peak appears at 235 °C, which can be ascribed to O_2^{2-} species, probably because Pt in contact with the CeO_2 domain promotes the formation of O_2^{2-}.[37] This phenomenon suggests that Pt species on Pt nanoparticles greatly promote the chemical adsorption of oxygen, probably through the transfer of electrons of the Pt d orbital to oxygen molecules. In the case of the Pt/CeO_2-WI sample, all oxygen desorption peaks become weak. Generally, surface oxygen of Ce-based catalysts is situated on the surface oxygen vacancy of CeO_2. According

https://doi.org/10.1021/acsomega.2c07399
ACS Omega 2023, 8, 6791−6800

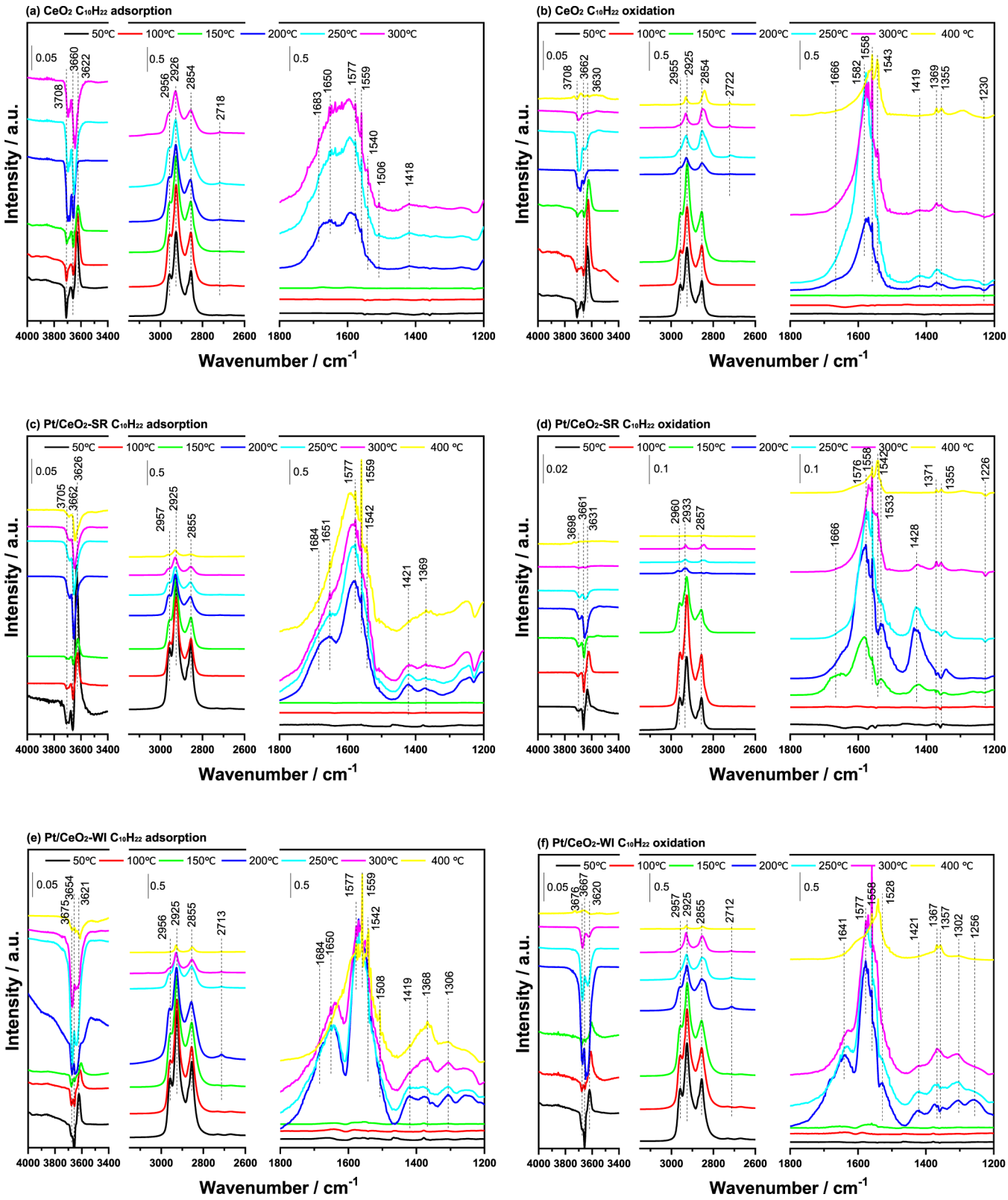

Figure 6. In situ FTIR in 1200−4000 cm^{-1} region for the adsorption and oxidation of $C_{10}H_{22}$ over CeO_2 (a,b), Pt/CeO_2-SR (c,d) and Pt/CeO_2-WI (e,f).

to Raman spectra, the difference in the band at 259 cm^{-1} (related to oxygen vacancy) for Pt/CeO_2-WI and Pt/CeO_2-SR is small, that is to say, a significant decrease in surface oxygen should be related to the other cause. Pt−O−Ce exists on CeO_2 as $Pt^{2+}(-O-Ce)_2$ or $Pt^{4+}(-O-Ce)_4$, which may shield oxygen vacancy, resulting in a decrease in the availability of oxygen vacancy and oxygen mobility.

2.5. In Situ FT-IR of $C_{10}H_{22}$, C_6H_{14}, and C_3H_8 Adsorption and Oxidation. For $C_{10}H_{22}$ adsorption on CeO_2 (Figure 6a), the bands at around 2956, 2926, and 2854

https://doi.org/10.1021/acsomega.2c07399
ACS Omega 2023, 8, 6791−6800

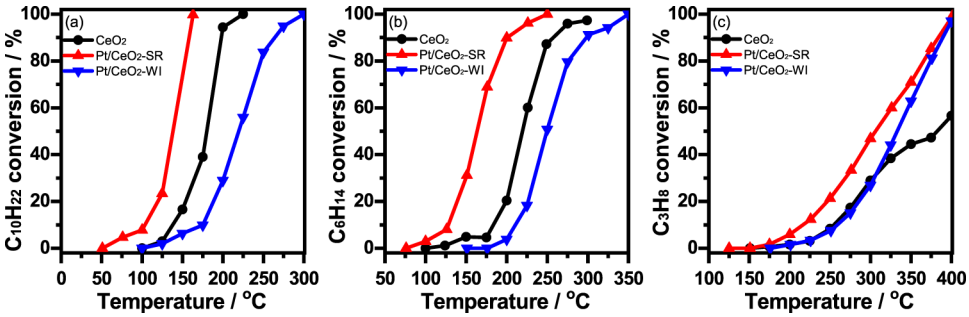

Figure 7. Catalytic oxidation of $C_{10}H_{22}$ (a), C_6H_{14} (b), and C_3H_8 (c) on CeO_2 and Pt/CeO_2 catalysts; gas compositions: 1000 ppm $C_{10}H_{22}$, or 1500 ppm C_6H_{14}, or 3000 ppm C_3H_8; 20% O_2 and N_2 balance; gas hour space velocity (GHSV): 30,000 h^{-1}; catalyst amount: 200 mg.

Table 2. Activities of Pt/CeO_2 Catalysts for $C_{10}H_{22}$, C_6H_{14}, and C_3H_8 Oxidation

catalyst	$C_{10}H_{22}$			C_6H_{14}			C_3H_8		
	T_{50}/°C	T_{90}/°C	rate[a] /μmol min^{-1} m^{-2}	T_{50}/°C	T_{90}/°C	rate[a]/μmol min^{-1} m^{-2}	T_{50}/°C	T_{90}/°C	rate[a]/μmol min^{-1} m^{-2}
CeO_2	182	198	0.031	220	257	0.058	384		0.257
Pt/CeO_2-SR	138	158	0.164	163	200	0.321	306	385	0.485
Pt/CeO_2-WI	220	264	0.014	250	299	0.016	334	389	0.418

[a]The apparent reaction rates at 150 °C for $C_{10}H_{22}$, at 200 °C for C_6H_{14} and at 350 °C for C_3H_8 under the reaction condition described in Figure 7.

cm^{-1} can be ascribed to the vibration of C-H of adsorbed $C_{10}H_{22}$,[38] while in the hydroxyl section, there appears a strong positive band at 3622 cm^{-1}, along with a broad negative band in 3714−3647 cm^{-1}. These bands become weak with the increase in temperature, and the bands at 1650 (C═O), 1577, 1559, and 1418 cm^{-1} (carboxylate species) become significant, indicating that the hydroxyl on the catalyst surface interacts with $C_{10}H_{22}$, resulting in the break of C−H, while the formation of intermediates containing oxygen (at 200 °C) is involved in surface oxygen. With oxygen addition, the bands ascribed to −OH and C−H quickly disappear at 200 °C, and the band at 1559 cm^{-1} grows in intensity greatly. This phenomenon suggests that the oxidation is promoted. With Pt particles loading on CeO_2 (Pt/CeO_2-SR), the adsorption of $C_{10}H_{22}$ in oxygen-containing feed becomes much weaker at low temperature (Figure 6d), probably due to the completion of oxygen with $C_{10}H_{22}$ for adsorption sites. The adsorption and activation of oxygen occur on Pt particles with Pt^0 species as low as 50 °C. The produced surface oxygen species transfer to $C_{10}H_{22}$ adsorption sites, the oxidation occurs. Moreover, the bands to carboxylate species appear significantly below 150 °C, where $C_{10}H_{22}$ of conversion approaches 100% in kinetic reaction (see later). Obviously, the activity of Pt/CeO_2-SR increases through the promotion of oxygen adsorption and activation. Similar $C_{10}H_{22}$ adsorption spectra on Pt/CeO_2-WI with Pt−O−Ce species are observed (Figure 6e,f), but oxygen addition cannot promote the oxidation, indicating that Pt of Pt−O−Ce species is not favorable for the oxygen activation on CeO_2. In the cases of C_6H_{14} and C_3H_8, the intensity of adsorption decreases significantly (Figures S5 and S6). Obviously, the number of carbon atoms in alkanes affects the behavior of adsorption on CeO_2. Probably, $C_{10}H_{22}$ adsorption involves in the interaction with multiple sites, which promotes the activation of $C_{10}H_{22}$, while the interaction with multiple sites becomes difficult with the decrease in carbon atoms.

2.6. Activity. The light-off curves of alkanes (HCs) over CeO_2 and Pt/CeO_2 catalysts are shown in Figure 7. The reactivity of HCs is characterized by T_{50} and T_{90} (at which the conversions reach 50 and 90%, respectively (Table 2)). It can be seen that the longer the chain length of HCs, the lower the temperature required for their oxidation. CeO_2 presents considerable activities with T_{50}/T_{90} of 182/198 °C for $C_{10}H_{22}$ (the rate at 150 °C of 0.031 μmol min^{-1} m^{-2}), and 220/257 °C for C_6H_{14} (the rate at 200 °C of 0.058 μmol min^{-1} m^{-2}), respectively. Pt addition by the solution reduction method (Pt/CeO_2-SR) greatly promotes the activity of CeO_2, and T_{50}/T_{90} decrease to 138/158 °C for $C_{10}H_{22}$ oxidation (the rate at 150 °C of 0.164 μmol min^{-1} m^{-2}), 163/200 °C for C_6H_{14} oxidation (the rate at 200 °C of 0.321 μmol min^{-1} m^{-2}). However, the activity of the Pt/CeO_2-WI catalyst for the oxidation of $C_{10}H_{22}$ and C_6H_{14} becomes lower, even than that of the CeO_2 catalyst. T_{50}/T_{90} values rise to 220−250/264−299 °C, and the rate significantly decreases to 0.014 μmol min^{-1} m^{-2} (at 150 °C) and 0.016 μmol min^{-1} m^{-2} (at 200 °C). Moreover, in C_3H_8 oxidation, the activity of CeO_2 is poor with T_{50} at 384 °C, and T_{90} is not available below 400 °C and the rate at 350 °C reaches 0.257 μmol min^{-1} m^{-2}. C_3H_8 conversion curves over Pt/CeO_2-SR and Pt/CeO_2-WI shift to low temperature with T_{50}/T_{90} values of 306/385 °C and 334/389 °C, respectively, and the rates at 350 °C increase to 0.485 and 0.418 μmol min^{-1} m^{-2}. The activity difference for C_3H_8 oxidation between two catalysts becomes small with the increase in temperature. It should be noted that Pt/CeO_2 catalysts have similar activity of C_3H_8 oxidation in the temperature range blow 300 °C. Considering the fact that the adsorption behavior of HCs on Pt/CeO_2-SR and Pt/CeO_2-WI catalysts is similar to that on CeO_2, it can be deduced that the exposed CeO_2 is responsible for the activation of HCs, probably through the interaction between C−H and Ce−OH, as shown in in situ FT-IR spectra of HC adsorption. Therefore, the activity order for $C_{10}H_{22}$ and C_6H_{14} oxidation of Pt/CeO_2-SR > Pt/CeO_2-WI can be ascribed to that the Pt/CeO_2-SR catalyst possesses better reducibility and high dissociation and activation of oxygen molecules. As reported,[39] the increase in the Pt particle size could decrease the energy of bonds between oxygen and Pt and promoted the mobility of oxygen species, due to low degree of coordination unsaturation of Pt atoms of

https://doi.org/10.1021/acsomega.2c07399
ACS Omega 2023, 8, 6791−6800

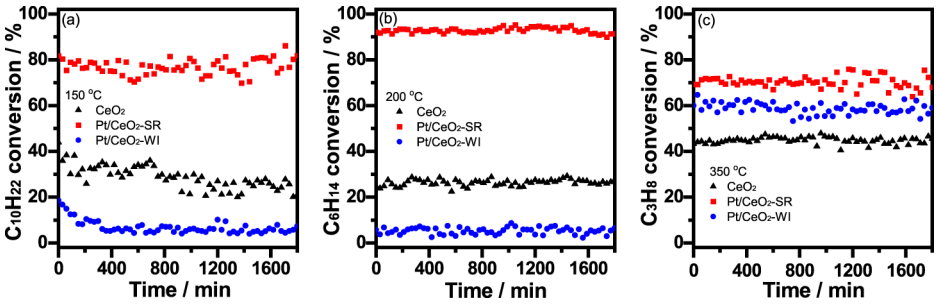

Figure 8. Activity for HC catalytic oxidation over CeO_2 and Pt/CeO_2 catalysts on stream feed at 150 °C (1000 ppm $C_{10}H_{22}$) (a), 200 °C (1500 ppm C_6H_{14}) (b), and 350 °C (3000 ppm C_3H_8) (c); 20% O_2 and N_2 balance; GHSV = 30,000 mL g^{-1} h^{-1}; catalyst amount: 200 mg.

Pt crystal planes on the surface of large particles. Moreover, the adsorption and activation of $C_{10}H_{22}$, C_6H_{14} and C_3H_8 on CeO_2 are dependent of their number of carbon atoms, which cooperate on multisites for adsorption with favorable geometry. Here, HCs with a small number of carbon atoms are often difficult for cooperation on CeO_2, probably due to unsuitable angle or chain length, and their adsorption and activation are rate-steps. As a result, Pt addition into CeO_2 almost cannot affect the activity of CeO_2 catalyst for the oxidation of HCs with small number of carbon atoms such as C_3H_8. In addition, the Pt/CeO_2-WI catalyst was treated with 10% H_2/N_2 at 450 °C for 4 h (noted as Pt/CeO_2-WI-R). The activity of the Pt/CeO_2-WI-R catalyst for $C_{10}H_{22}$ oxidation is promoted (Figure S7), and T_{50}/T_{90} decreases to 180/240 °C. However, raising temperature up to 180 °C, the conversion curve shifts to high temperature, and the temperature of 100% conversion is close to that obtained on the Pt/CeO_2-WI catalyst, which is probably related to the reduction of Pt species with $C_{10}H_{22}$. Indeed, the reduced Pt species of Pt−O−Ce can be reoxidized easily, which is confirmed by XPS spectra (Figure S8).

2.7. Stability Tests. The stability of catalysts was tested on the feed stream containing 1000 ppm $C_{10}H_{22}$, 1500 ppm C_6H_{14} and 3000 ppm C_3H_8, respectively (here, maintaining the number of C atom to be almost same) (Figure 8). In $C_{10}H_{22}$ oxidation at 150 °C, the Pt/CeO_2-SR catalyst shows 80% stable conversion within 1800 min duration, while Pt/CeO_2-WI and CeO_2 catalysts deactivate with the decrease in conversion from 20% to 6% within initial 300 min, and from 38 to 22% within 1800 min, respectively. As seen in FT-IR spectra during $C_{10}H_{22}$ adsorption, the band at 1582 cm^{-1} ascribed to C═C of benzene appears. If the oxidation of benzene-like compounds is not quick, and their condensation can occur easily, finally resulting in carbon deposition on the catalysts. The Pt/CeO_2-SR catalyst is active for oxidation at low temperature, due to high availability of active surface oxygen. The deactivation resulting from benzene-like compounds can be avoided. Stable conversions of C_6H_{14} (200 °C) and C_3H_8 (350 °C) maintain at 6, 90 and 25%, and 42, 60 and 70% within 1800 min over CeO_2, Pt/CeO_2-SR, and Pt/CeO_2-WI catalysts, respectively. These results are related to quick oxidation at high temperature. XPS analyses of used catalysts in $C_{10}H_{22}$ oxidation show that there is no significant change in binding energies of Pt and Ce, but Pt^0 species of Pt catalysts increases obviously (Figure S9a), indicating that oxidized Pt species is reduced to Pt^0 species partially with $C_{10}H_{22}$, as seen in C_3H_8 catalytic combustion.[40] With 2% V/V H_2O into the feed, the Pt/CeO_2-SR catalyst presents the slightly decreased activity for $C_{10}H_{22}$ (150 °C) and C_6H_{14} (200 °C) oxidation, and stable conversion within 400 min duration decreases to 71 and 87% from 80 and 90% respectively (Figures S10 and 9),

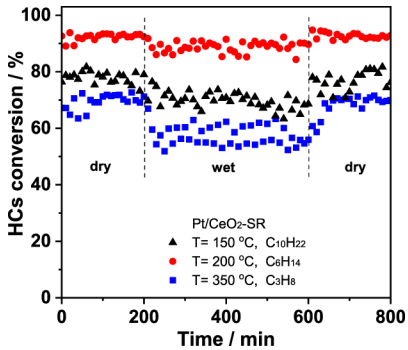

Figure 9. Stability of the Pt/CeO_2-SR catalyst in $C_{10}H_{22}$, C_6H_{14}, and C_3H_8 oxidation in dry and wet feed (containing 2% V/V water); gas compositions: 1000 ppm $C_{10}H_{22}$, or 1500 ppm C_6H_{14}, or 3000 ppm C_3H_8; 20% O_2 and N_2 balance; GHSV = 30,000 mL g^{-1} h^{-1}; catalyst amount: 200 mg.

while the deactivation for C_3H_8 oxidation becomes significant with stable conversion at 350 °C within 300 min decreases to 57% from 70% in dry feed. Turning off water, the conversion quickly returns to the level in dry feed. These results suggest that the deactivation caused by water is reversible. In addition, the reported results of metal oxide catalysts for $C_{10}H_{22}$, C_6H_{14} and C_3H_8 oxidation were listed in Table S3. The Pt/CeO_2-SR catalyst presents excellent performance in a broad range of reactant concentrations, including high activity, stability, will be desirable for industrial applications.

2.8. Effect of Reactant Concentration on the Activity. Maintaining $C_{10}H_{22}$, C_6H_{14}, and C_3H_8 concentration at 1000, 1500, and 3000 ppm individually in the corresponding feed, oxygen concentration ($[O_2]$) is changed in a range of 2−20%. Considering that the stoichiometric $[O_2]$ values are 1.55%, 1.425%, and 1.5%, respectively, for $C_{10}H_{22}$, C_6H_{14}, and C_3H_8 oxidation, the effect of $[O_2]$ on the activity of CeO_2, Pt/CeO_2-SR, and Pt/CeO_2-WI catalysts in the fuel-lean region is investigated (Figure 10). At 2, 5, 10, and 20%, T_{90} of $C_{10}H_{22}$ over the Pt/CeO_2-SR catalyst is 237, 196, 166, and 158 °C (Figure S11), while the conversion at 150 °C is 10, 18, 52, and 74%. Obviously, the reaction at 150 °C in 1000 ppm $C_{10}H_{22}$ feed is kinetically controlled, and the dependency of reaction on $[O_2]$ is near the first order. That is to say, $C_{10}H_{22}$ adsorption is quick enough to meet the oxidation step. For the Pt/CeO_2-WI catalyst, T_{90} rises up to 264−313 °C, and the conversion at 150 °C decreases to 0−6% in the same $[O_2]$ range. As above mentioned, the adsorption and activation of

https://doi.org/10.1021/acsomega.2c07399
ACS Omega 2023, 8, 6791−6800

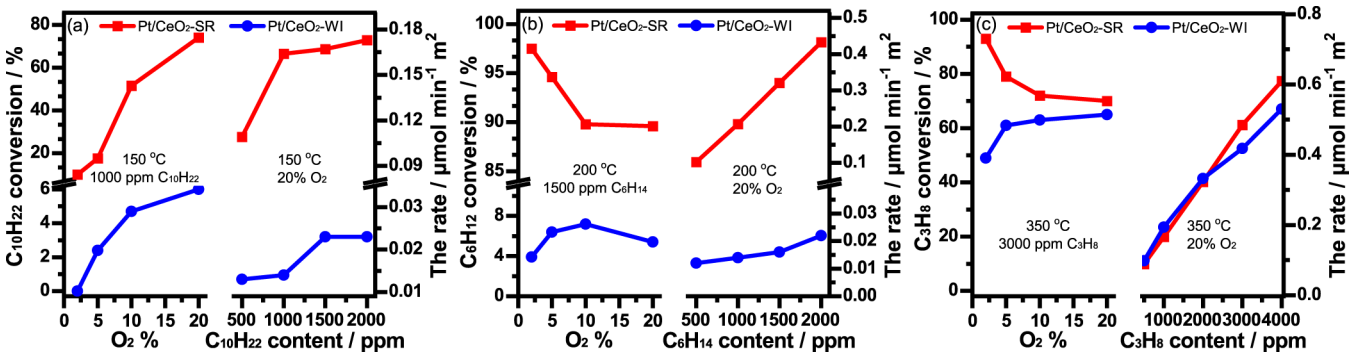

Figure 10. $C_{10}H_{22}$ (a), C_6H_{14} (b), and C_3H_8 (c) conversion at various O_2 concentrations and the rate at various HCs concentrations maintaining 20% O_2 over Pt/CeO_2-SR and Pt/CeO_2-WI catalysts; GHSV = 30,000 mL g^{-1} h^{-1}; catalyst amount: 200 mg.

$C_{10}H_{22}$ can occur at 150 °C, where the adsorption of oxygen molecules is limited on CeO_2 with Pt−O−Ce species, even raising [O_2], because of strong bonding between Pt and oxygen. Raising temperature, the different phenomenon is observed in the oxidation of C_6H_{14} and C_3H_8. Over the Pt/CeO_2-SR catalyst, in the 2−20% [O_2] range, C_6H_{14} conversion at 200 °C decreases to 97−90%, and C_3H_8 conversion at 350 °C, to 93−70%. With the activation of oxygen at high temperature, surface oxygen competes with HC molecules for adsorption sites on the catalyst surface, resulting in the decrease in activated HC molecules. While for Pt/CeO_2-WI catalyst, because oxygen activation capacity is not large enough to compete with HC molecules for adsorption sites, the increase in [O_2] is favorable for the oxidation. Increasing $C_{10}H_{22}$, C_6H_{14}, and C_3H_8 concentration from 500 ppm to 2000, 2000, and 4000 ppm, respectively, and maintaining [O_2] at 20%, the reactant conversion curves shift to high temperature (Figure S12), but the reaction rates of HCs (at 150, 200, and 350 °C for $C_{10}H_{22}$, C_6H_{14}, and C_3H_8, respectively) increases to a different extent (Figure 10). Considering that O_2/HCs ratios are far greater than the theoretical ratio, the increase in the reaction rate with HC concentration can be ascribed to the dependency of reaction on reactant.

3. CONCLUSIONS

Pt catalysts supported on CeO_2 prepared by the solution reduction method and wet impregnation method were used in the oxidation of $C_{10}H_{22}$, C_6H_{14}, and C_3H_8. Pt species on the Pt/CeO_2-SR sample present Pt nanoparticles with Pt^{2+} and Pt^0, while highly dispersed Pt^{2+} and Pt^{4+} species exist on the Pt/CeO_2-WI sample in the form of Pt−O−Ce. High reducibility and mobility of oxygen species are observed on Pt nanoparticles, which results from high activity for the adsorption and activation of oxygen. The reducibility of the Pt/CeO_2-WI sample with Pt−O−Ce decreases to a significant extent, compared with CeO_2. In situ FT-IR shows that $C_{10}H_{22}$ as a long chain alkane model can adsorb as low as 50 °C on the CeO_2 domain through the interaction with Ce−OH (which is confirmed by the negative hydroxyl band). Surface active oxygen can compete with $C_{10}H_{22}$ for adsorption sites. The Pt/CeO_2-SR sample presents high activity for $C_{10}H_{22}$ oxidation, due to high ability of Pt nanoparticles for adsorption and activation of oxygen. The adsorption of C_6H_{14} and C_3H_8 on the CeO_2 domain becomes much weaker, resulting in low activity for their oxidation. In kinetic oxidation of $C_{10}H_{22}$, C_6H_{14}, and C_3H_8, the Pt/CeO_2-SR catalyst shows the highest activity with T_{90} of 158, 200, and 385 °C, respectively, really due to its high availability of active surface oxygen. The difference in reactivity of $C_{10}H_{22}$, C_6H_{14}, and C_3H_8 can be ascribed to their different adsorption behavior, which results from the number of carbon atoms contacted with CeO_2 domain. At 20% oxygen content, the rates of $C_{10}H_{22}$, C_6H_{14} and C_3H_8 oxidation increase with their contents. CeO_2 and Pt/CeO_2-WI catalysts present the decreased activity, due to their low availability of surface oxygen. Stability investigation of catalysts in feed stream shows that 80% $C_{10}H_{22}$ conversion on Pt/CeO_2-SR catalyst at 150 °C can maintain for 1800 min duration. While the deactivation of CeO_2 and Pt/CeO_2-WI catalysts suggests that slow oxidation of $C_{10}H_{22}$ adsorption intermediates results in carbon deposition. Raising temperature to 200 °C or higher, the stable activity for C_6H_{14} and C_3H_8 oxidation over three catalysts can be obtained.

4. EXPERIMENTAL SECTION

4.1. Catalyst Preparation. CeO_2 was prepared by a hydrothermal method. $Ce(NO_3)_3{\cdot}6H_2O$ (10 g) and urea (3 g) were dissolved in deionized water (40 mL) under stirring for 30 min at room temperature, and then the obtained solution was moved into a Teflon-lined stainless-steel autoclave (100 mL) and heated up to 140 °C for 300 min. After cooling to room temperature, the formed precipitate was washed with 2 L deionized water and ethanol, dried at 110 °C overnight, and finally thermally treated at 450 °C in an air atmosphere for 240 min.

Pt/CeO_2 catalysts were prepared by two different methods. For the solution reduction technique, typically, 2 g of the above obtained CeO_2 was dispersed in 10 mL of deionized water, and then 1 mL of 0.2 M H_2PtCl_6 aqueous solution was added (1.0 wt % Pt to CeO_2) to form a suspension. The mixture was magnetically stirred for 2 h at room temperature. Subsequently, 1 mL of hydrazine hydrate (60%) was dropwise added as a reducing agent. The mixture solution was stirred for 20 min at 70 °C. After that, the precipitate was washed with 1 L of deionized water and dried at 110 °C overnight. For the wet impregnation method, 2 g of the above obtained CeO_2 was immersed in 1 mL aqueous solution of H_2PtCl_6 (0.2 M). Then, the sample was dried at 110 °C overnight. Finally, the samples were thermally treated at 450 °C in an air atmosphere for 240 min. The obtained powders were denoted as Pt/CeO_2-SR and Pt/CeO_2-WI, respectively.

4.2. Catalyst Characterization. The X-ray diffraction (XRD, D/MAX 2550 VB/PC, Cu Ka radiation) technique was used to study the crystal structure and phase of the samples.

https://doi.org/10.1021/acsomega.2c07399
ACS Omega 2023, 8, 6791−6800

The diffractogram was recorded in a 2θ range of 10−80° with a 2θ step of 0.01° and a time step of 10 s. The actual Pt loading was determined by ICP-OES. The nitrogen adsorption−desorption isotherm was measured statically at 77 K on an ASAP 2460 system. The sample was pretreated thermally at 200 °C for 12 h. The surface area of the sample was estimated with the BET model. TEM/HRTEM images were taken on a JEM-2100F field emission transmission electron microscope. Raman spectra were recorded with a laser micro-Raman spectrometer system equipped with a confocal microscope, notch filter (532 nm), and a single-stage monochromator. XPS was conducted on a Thermo ESCALAB 250XI spectrometer using Al K_α (1486.6 eV) radiation as the excitation source to obtain the spectra Pt 4f, Ce 3d, and O 1s of the samples.

The Pt dispersion was determined on a Micromeritics AutochemII2920 by the cryogenic CO pulse adsorption method. For prereduced procedure, 5% H_2/Ar was fed to sample at 30 mL/min at 300 °C for 30 min. Then the sample was cooled to −50 °C in Ar flow with a liquid nitrogen device. Then, 0.5173 mL of 1% CO/Ar was pulsed every 5 min until the intensity of the CO peak was constant to obtain the curves. Pt dispersion and mean particle diameter were calculated according to the literature.[24]

H_2-TPR was investigated by heating catalysts (100 mg) in H_2/Ar (5%) flow (30 mL·min^{-1}) at a heating rate of 10 °C·min^{-1} from −50 to 800 °C. Before the H_2-TPR analyses, samples were heated for 60 min in Ar flow at 200 °C. The quantitative result of the area under a reduction peak was calibrated on the basis of hydrogen consumption from the reduction of CuO to Cu.

The O_2-TPD was tested by Micromeritics AutochemII 2920 equipped with a quadrupole mass detector. Typically, the sample (100 mg) was pretreated at 400 °C with He flow (30 mL/min) for 60 min and then cooled down to 90 °C, followed by treatment with O_2/He (2%) flow (30 mL/min) for 30 min. After being purged with He flow (30 mL/min) for 30 min, the sample was heated from 90 to 700 °C in He flow (30 mL/min) at a heating rate of 10 °C/min.

A Nicolet 6700 FT-IR equipped with a liquid nitrogen-cooled mercury-cadmium-telluride (MCT) detector was used in the in situ DRIFTS test. The DRIFTS cell (Harrick, HVC-DRP) equipped with CaF_2 windows was used as the reaction chamber that allowed the samples to be heated to 600 °C. All the spectra were within the range of 4000−1200 cm^{-1} at a resolution of 4 cm^{-1} and 64 scans. Before CO adsorption, the sample was pretreated at 200 °C for 60 min in Ar atmosphere.

After the pretreatment, the temperature was cooled to 30 °C and the background spectra were recorded, then CO adsorption was carried out under the atmosphere of CO/Ar (1%) until the adsorption signal did not change. The gas was switched to Ar to remove most of the gaseous CO and then adsorption spectra was collected.

For hydrocarbon adsorption, the sample was pretreated by flowing 20% O_2/Ar flow at 400 °C for 60 min with the subsequent exposure to 1000 ppm $C_{10}H_{22}$/Ar or 1500 ppm C_6H_{14}/Ar or 3000 ppm C_3H_8/Ar feed to reach saturation at various temperature and then to Ar for 30 min, and finally FT-IR spectra were recorded. For hydrocarbon oxidation, the sample was pretreated at 400 °C by flowing 20% O_2/Ar for 2 h with subsequent exposure to the feed of 20% O_2/Ar containing 1000 ppm $C_{10}H_{22}$ or 1500 ppm C_6H_{14} or 3000 ppm C_3H_8 to reach saturation at various temperatures. After purging the sample with 20% O_2/Ar for 30 min, the corresponding spectrum was recorded.

4.3. Catalyst Activity Measurements. The activity and stability of catalysts for catalytic oxidation of hydrocarbon were investigated in a tubular quartz reactor (4 mm diameter). The particle mixture (40−60 mesh) of 200 mg catalyst was placed on the reactor bed, through which the feed composed of 2−20% O_2/N_2 containing 500−4000 ppm reactant flowed at 100 mL min^{-1} at 30,000 mL g^{-1} h^{-1} GHSV. The temperature was controlled at 50−500 °C. On-line analyses for organic compounds were conducted with GC (GC2060) equipped with a flame ionization detector (FID) and a ffap-30 m × 0.32 mm × 0.50 μm capillary column. Considering negligible change in the feed volume during the reaction, the conversion was calculated by the difference between initial and final reactant concentrations divided by initial reactant concentration. No byproducts other than H_2O and CO_2 were detected by GC.

■ ASSOCIATED CONTENT

Supporting Information

The Supporting Information is available free of charge at https://pubs.acs.org/doi/10.1021/acsomega.2c07399.

Materials characterization; the reported activities of metal oxide catalysts for $C_{10}H_{22}$, C_6H_{14} and C_3H_8 oxidation; N_2 sorption isotherms and pore size distributions; TEM, HRTEM images; HAADF-STEM-EDX element-mapping analyses of Pt; XPS spectra of Ce 3d and O 1s; FTIR spectra of C_6H_{14} and C_3H_8 adsorption and oxidation; XPS spectra of Pt 4f and Ce 3d of the used catalysts; $C_{10}H_{22}$ conversion curves over the Pt/CeO_2-WI-R catalyst; XPS spectra of the Pt 4f of Pt/CeO_2-WI-R catalyst; the activity of $C_{10}H_{22}$, C_6H_{14}, and C_3H_8 oxidation over the Pt/CeO_2-SR catalyst in wet feed; $C_{10}H_{22}$, C_6H_{14}, and C_3H_8 conversion curves at various O_2 concentrations and HC concentrations (PDF)

■ AUTHOR INFORMATION

Corresponding Author

Xingyi Wang − *Research Institute of Industrial Catalysis, School of Chemistry and Molecular Engineering, East China University of Science and Technology, Shanghai 200237, PR China;* orcid.org/0000-0003-3505-6111; Email: wangxy@ecust.edu.cn

Authors

Xiaohui Gao − *Research Institute of Industrial Catalysis, School of Chemistry and Molecular Engineering, East China University of Science and Technology, Shanghai 200237, PR China*

Yuting Bai − *Research Institute of Industrial Catalysis, School of Chemistry and Molecular Engineering, East China University of Science and Technology, Shanghai 200237, PR China*

Hao Zhang − *Research Institute of Industrial Catalysis, School of Chemistry and Molecular Engineering, East China University of Science and Technology, Shanghai 200237, PR China*

Complete contact information is available at: https://pubs.acs.org/10.1021/acsomega.2c07399

https://doi.org/10.1021/acsomega.2c07399
ACS Omega 2023, 8, 6791−6800

Notes

The authors declare no competing financial interest.

■ ACKNOWLEDGMENTS

We would like to acknowledge the National Natural Science Foundation of China (no. 21976056, 21777043, and 21922602).

■ REFERENCES

(1) Ventura, A.; Jullien, A.; Moneron, P. Polycyclic aromatic hydrocarbons emitted from a hot-mix drum, asphalt plant: study of the influence from use of recycled bitumen. *J. Environ. Eng. Sci.* **2007**, *6*, 727−734.

(2) Kittelson, D. B. Engines and nanoparticles: a Review. *J. Aerosol Sci.* **1998**, *29*, 575−588.

(3) Spivey, J. J. Complete catalytic oxidation of volatile organics. *Ind. Eng. Chem. Res.* **1987**, *26*, 2165−2180.

(4) Hutchings, G. J.; Heneghan, C. S.; Hudson, I. D.; Taylor, S. H. Uranium-oxide-based catalysts for the destruction of volatile chloro-organic compounds. *Nature* **1996**, *384*, 341−343.

(5) Zuo, S.; Wang, X.; Yang, P.; Qi, C. Preparation and high performance of rare earth modified Pt/MCM-41 for benzene catalytic combustion. *Catal. Commun.* **2017**, *94*, 52−55.

(6) Wu, J.; Chen, B.; Yan, J.; Zheng, X.; Wang, X.; Deng, W.; Dai, Q. Ultra-active Ru supported on CeO_2 nanosheets for catalytic combustion of propane: Experimental insights into interfacial active sites. *Chem. Eng. J.* **2022**, *438*, No. 135501.

(7) Du, J.; Li, H.; Wang, C.; Zhang, A.; Zhao, Y.; Luo, Y. Improved catalytic activity over P-doped ceria-zirconia-alumina supported palladium catalysts for methane oxidation. *Catal. Commun.* **2020**, *141*, No. 106012.

(8) Cao, C.; Yang, H.; Xiao, J.; Yang, X.; Ren, B.; Xu, L.; Liu, G.; Li, X. Catalytic diesel soot elimination over potassium promoted transition metal oxide (Co/Mn/Fe) nanosheets monolithic catalysts. *Fuel* **2021**, *305*, No. 121446.

(9) Li, J.; Hua, J.; Shi, Y.; Zhao, J.; Wang, H.; Deng, S.; Cui, Y.; Wang, F.; Long, H.; Tan, Y. The reaction mechanism of highly dispersed Cu atoms and ultrafine MnO_x nanoclusters co-modified ZSM-5 based on In-situ heteronuclear substitution for catalytic oxidation C_6H_{14}. *Chem. Eng. J.* **2023**, *451*, No. 138721.

(10) Peng, C.; Yu, D.; Zhang, C.; Chen, M.; Wang, L.; Yu, X.; Fan, X.; Zhao, Z.; Cheng, K.; Chen, Y.; Wei, Y.; Liu, J. Alkali/alkaline earth-metal-modified MnO_x supported on three-dimensionally ordered macroporous-mesoporous $Ti_xSi_{1-x}O_2$ catalysts: Preparation and catalytic performance for soot combustion. *J. Environ. Sci.* **2023**, *125*, 82−94.

(11) Santos, V. P.; Carabineiro, S. A. C.; Tavares, P. B.; Pereira, M. F. R.; Órfão, J. J. M.; Figueiredo, J. L. Oxidation of CO, ethanol and toluene over TiO_2 supported noble metal catalysts. *Appl. Catal., B* **2010**, *99*, 198−205.

(12) Gololobov, A. M.; Bekk, I. E.; Bragina, G. O.; Zaikovskii, V. I.; Ayupov, A. B.; Telegina, N. S.; Bukhtiyarov, V. I.; Stakheev, A. Y. Platinum nanoparticle size effect on specific catalytic activity in n-alkane deep oxidation: Dependence on the chain length of the paraffin. *Kintet. Catal.* **2009**, *50*, 830.

(13) Masaaki, H.; Motoi, S.; Hideaki, H.; Masakuni, O. Effect of Pt dispersion on the catalytic activity of supported Pt catalysts for diesel hydrocarbon oxidation. *Top. Catal.* **2013**, *56*, 249−254.

(14) Fabrice, D.; Jacques, B., Jr.; Daniel, D.; Isabelle, G.; Gil, M. Catalytic oxidation of heavy hydrocarbons over Pt/Al_2O_3: Influence of the structure of the molecule on its reactivity. *Appl. Catal., B* **2010**, *95*, 217−227.

(15) Ya-Huei, C.; Corneliu, B.; Matthew, N.; Enrique, I. Reactivity of chemisorbed oxygen atoms and their catalytic consequences during CH_4-O_2 catalysis on supported Pt clusters. *J. Am. Chem. Soc.* **2011**, *133*, 15958−15978.

(16) Mónica, G.; Ya-Huei, C.; Enrique, I. Catalytic reactions of dioxygen with ethane and methane on platinum clusters: Mechanistic connections, site requirements, and consequences of chemisorbed oxygen. *J. Catal.* **2012**, *285*, 260−272.

(17) Casey, P. O.; Glen, R. J.; Dong, H.; Dionisios, G. V.; Ivan, C. L. Deactivation of Pt/Al_2O_3 during propane oxidation at low temperatures: Kinetic regimes and platinum oxide formation. *J. Catal.* **2016**, *337*, 122−132.

(18) Chiba, A.; Komoda, M.; Kosumi, T.; Nanba, T.; Azuma, N.; Ueno, A. Difference in catalytic combustion of propane and propene on Pt/Al_2O_3 catalyst. *Chem. Lett.* **1999**, *28*, 801−802.

(19) Hasan, M. A.; Zaki, M. I.; Pasupulety, L. IR investigation of the oxidation of propane and likely C3 and C2 products over Group IVB metal oxide catalysts. *J. Phys. Chem. B* **2002**, *106*, 12747−12756.

(20) Oliviero, L.; Barbier, J., Jr.; Labruquére, S.; Duprez, D. Role of the metal−support interface in the total oxidation of carboxylic acids over Ru/CeO_2 catalysts. *Catal. Lett.* **1999**, *60*, 15−19.

(21) Ding, K.; Ahmet, G.; Johnson, A. M.; Schweitzer, N. M.; Galen, D. S.; Laurence, D. M.; Peter, C. S. Identification of active sites in CO oxidation and water-gas shift over supported Pt catalysts. *Science* **2015**, *350*, 189−192.

(22) Dong, J.; Li, D.; Zhang, Y.; Chang, P.; Jin, Q. Insights into the CeO_2 facet-depended performance of propane oxidation over Pt-CeO_2 catalysts. *J. Catal.* **2022**, *407*, 174−185.

(23) Nie, R.; Liang, D.; Shen, L.; Gao, J.; Chen, P.; Hou, Z. Selective oxidation of glycerol with oxygen in base-free solution over MWCNTs supported PtSb alloy nanoparticles. *Appl. Catal., B* **2012**, *127*, 212−220.

(24) Shin'ichi, K.; Yoshiteru, Y.; Atsushi, S.; Tadashi, H. Determination of metal dispersion of Pt/CeO_2 catalyst by CO-pulse method. *J. Jpn. Pet. Inst.* **2005**, *48*, 173−177.

(25) Weber, W. H.; Hass, K. C.; McBride, J. R. Raman study of CeO_2: Second-order scattering, lattice dynamics, and particle-size effects. *Phys. Rev. B* **1993**, *48*, 178.

(26) Lin, W.; Herzing, A. A.; Kiely, C. J.; Wachs, I. E. Probing metal−support interactions under oxidizing and reducing conditions: In situ Raman and infrared spectroscopic and scanning transmission electron microscopic−X-ray energy-dispersive spectroscopic investigation of supported platinum catalysts. *J. Phys. Chem. C* **2008**, *112*, 5942−5951.

(27) McBride, J. R.; Graham, G. W.; Peters, C. R.; Weber, W.; Weber, H. Growth and characterization of reactively sputtered thin-film platinum oxides. *J. Appl. Phys.* **1991**, *69*, 1596.

(28) Marlène, D.; Stéphane, L. Probing reoxidation sites by in situ Raman spectroscopy: Differences between reduced CeO_2 and Pt/CeO_2. *Raman Spectrosc.* **2012**, *43*, 1312−1319.

(29) Tong, T.; Liu, X.; Guo, Y.; Banis, M.; Hu, Y.; Wang, Y. The critical role of CeO_2 crystal-plane in controlling Pt chemical states on the hydrogenolysis of furfuryl alcohol to 1,2-pentanediol. *J. Catal.* **2018**, *365*, 420−428.

(30) Prabhuram, J.; Zhao, T.; Wong, C.; Guo, J. Synthesis and physical/electrochemical characterization of Pt/C nanocatalyst for polymer electrolyte fuel cells. *J. Power Sources* **2004**, *134*, 1.

(31) Duarte, R. B.; Damyanova, S.; de Oliveira, D. C.; Marques, C. M. P.; Bueno, J. M. C. Study of Sm_2O_3-doped CeO_2-Al_2O_3-supported Pt catalysts for partial CH_4 oxidation. *Appl. Catal., A* **2011**, *399*, 134−145.

(32) Klaus-Dieter, S. Ordered ultra-thin cerium oxide overlayers on Pt(111) single crystal surfaces studied by LEED and XPS. *Surf. Sci.* **1998**, *399*, 29−38.

(33) Yao, H.; Yao, Y. Ceria in automotive exhaust catalysts: I. Oxygen Storage. *J. Catal.* **1984**, *86*, 254−265.

(34) Lee, J.; Ryou, Y.; Chan, X.; Kim, T. J.; Kim, D. H. How Pt interacts with CeO_2 under the reducing and oxidizing environments at elevated temperature: the origin of improved thermal stability of Pt/CeO_2 compared to CeO_2. *J. Phys. Chem. C* **2016**, *120*, 25870−25879.

(35) Sanchez, M. G.; Gazquez, J. L. Oxygen vacancy model in strong metal-support interaction. *J. Catal.* **1987**, *104*, 120−135.

(36) Masaoki, I.; Enrique, I. Mechanistic assessments of NO oxidation turnover rates and active site densities on WO_3-promoted CeO_2 catalysts. *J. Catal.* **2016**, *342*, 84−97.

https://doi.org/10.1021/acsomega.2c07399
ACS Omega 2023, 8, 6791−6800

(37) Gu, Y.; Shao, S.; Sun, W.; Xia, H.; Gao, X.; Dai, Q.; Zhan, W.; Wang, X. The oxidation of chlorinated organic compounds over W-modified Pt/CeO_2 catalysts. *J. Catal.* **2019**, *380*, 375−386.
(38) Pinkley, L. W.; Sethna, P. P.; Williams, D. Infrared band intensities of saturated hydrocarbons. *J. Phys. Chem.* **1978**, *82*, 1533.
(39) Patrick, B.; Aline, A.; Denis, J.; Michel, P. Effect of particle size on the reactivity of oxygen-adsorbed platinum supported on alumina. *Appl. Catal.* **1990**, *59*, 141−152.
(40) Zhao, P.; Chen, J.; Yu, H.; Cen, B.; Wang, W.; Luo, M.; Lu, J. Insights into propane combustion over MoO_3 promoted Pt/ZrO_2 catalysts: the generation of Pt-MoO_3 interface and its promotional role on catalytic activity. *J. Catal.* **2020**, *391*, 80−90.

https://doi.org/10.1021/acsomega.2c07399
ACS Omega 2023, 8, 6791−6800